Microwave Phase Modulators for Smoothing by Spectral Dispersion

A principal component of smoothing by spectral dispersion (SSD) is an electro-optic phase modulator that produces a cyclic wavelength modulation on nanosecond laser pulses. This article addresses the theory, design, manufacture, testing, and implementation of microwave phase modulators operating in the gigahertz-frequency range with particular application to both one- and two-dimensional SSD on the OMEGA laser system.

The first references in the literature to electro-optic modulators in the microwave-frequency range were in the early 1960s in applications of both amplitude and phase modulators to the recently invented laser. Most of these devices were wideband devices operating over the band from dc to some upper cutoff frequency for analog modulation[1] or over some narrow radio-frequency RF band for digital communications.[2] Early work concentrated on frequency-shifting laser beams for spectroscopic applications, especially FM heterodyne spectroscopy, but was usually confined to continuous-wave (cw) gas lasers, as well as some applications to temporal compression of short pulses generated by cw mode-locked gas laser oscillators.[3]

No work appears to have been done on modulators of the type needed for SSD that must impress relatively large bandwidths (several Å) in a single pass through an electro-optic crystal of relatively large cross section. Commercially available, guided-wave phase modulators can achieve large modulation bandwidths; however, the small cross section of these devices and the relatively low damage threshold of electro-optic materials are incompatible with the relatively high-power laser pulses typical in driver lines of large glass lasers used for inertial confinement fusion (ICF) applications. Furthermore, bulk electro-optic modulators enable the technique of "color cycling," which is critical to the successful implementation of SSD.[4]

SSD phase modulators have been employed on the OMEGA laser in several configurations. Originally, resonant modulators in the 2- to 3-GHz regime were employed in a scheme now identified as one-dimensional smoothing by spectral dispersion (1-D SSD).[5] In this scheme, a bandwidth is generated by a single modulator, and dispersion is applied along a single direction. Bandwidths of up to 2 Å were achieved with these original modulators. A higher-frequency modulator operating around 9 GHz was also operated in this configuration that achieved bandwidths in excess of 8.5 Å.

Two-dimensional SSD (2-D SSD) is currently implemented on OMEGA. This configuration involves two separate stages of gratings and modulators that apply dispersion in two orthogonal directions. Incommensurate modulation frequencies (3.0 and 3.3 GHz) are chosen for the two modulators to maximize the spectral content of the phase-modulated laser beam.

In the following sections, we present (1) the basic theory involved in microwave phase modulators; (2) computer simulations that used *SUPERFISH* to design the SSD modulators; (3) a review of the technical design criteria leading to the current modulator designs; and finally, (4) the testing results for these devices.

Theory

Phase modulation of laser pulses increases the bandwidth of laser pulses without introducing intensity modulation to the laser pulse that could be destructive to the glass laser system. The electric field of a phase-modulated pulse takes the form[6]

$$E(t) = E_0(t)\, e^{i\omega_0 t}\, e^{i\Phi(t)},$$

where $E_0(t)$ represents the pulse shape before phase modulation, ω_0 is the fundamental angular frequency of the laser, and $\Phi(t)$ is the time-varying phase. Since the laser intensity varies as $|E(t)|^2 = |E_0(t)|^2$, intensity modulation is avoided. The time-varying phase is achieved by passing the laser beam through an electro-optic crystal with an oscillating voltage applied across it. The resulting electric field of the laser beam is of the form

$$E(t) = E_0(t)e^{i\omega_0 t + i\eta\sin(\omega_m t)} = E_0(t)e^{i\omega_0 t}\sum_{n=-\infty}^{\infty} J_n(\eta)e^{i(\omega_0 + n\omega_m t)}, \quad (1)$$

where η is the phase-modulation amplitude and ω_m is the angular frequency of the modulation. The added bandwidth can be expressed as a Bessel-series expansion of the sinusoidal phase term, or frequency sidebands separated by the modulation frequency. The frequency bandwidth impressed by the phase modulation is conveniently characterized by $\Delta f = 2\eta f_m$, at which point the mode amplitudes $J_n(\eta)$ rapidly approach zero. For light near 1-μm wavelength, a bandwidth of 30 GHz corresponds to approximately $\Delta\lambda = 1$ Å.

The modulation amplitude η for a transverse-field, $LiNbO_3$ phase modulator shown in Fig. 68.25 is given by[6]

$$\eta = \frac{\pi \cdot \beta \cdot n_3^3\, r_{33}\,(V/T)L}{\lambda}, \quad (2)$$

where L is the length of the $LiNbO_3$ crystal in the direction of laser propagation, T is the thickness in the direction of the oscillating voltage, and W is the width. The reduction factor β accounts for phase mismatch between the propagating optical and microwave fields in the crystal, n_3 is the index of refraction for the optical field polarized parallel to the c-axis of $LiNbO_3$, r_{33} is the electro-optic coefficient, V_{applied} is the microwave voltage applied along the crystalline axis of the crystal, and λ is the wavelength of the laser light.

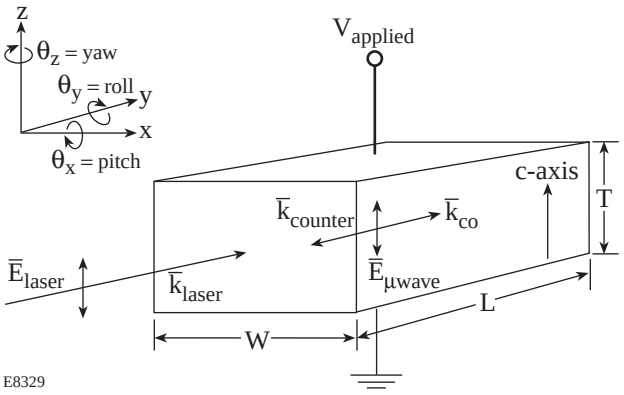

Figure 68.25
Geometry of $LiNbO_3$ crystal used in phase modulator.

The phase-mismatch reduction factor β is the usual term characteristic of nonlinear optical processes. In the resonant microwave cavities used for SSD phase modulators, microwave standing waves are impressed across the electro-optic crystal that can be decomposed into fields co-propagating $(\bar{k}_{\text{co}})$ and counter-propagating $(\bar{k}_{\text{counter}})$ with the laser beam. The phase-mismatch reduction factor is given by[7]

$$\beta = \frac{1}{2}\left|\frac{\sin(u_+)}{u_+} + \frac{\sin(u_-)}{u_-}\right|, \quad (3a)$$

and

$$u_\pm = \left(\frac{\pi\, f_m\, L}{c}\right)\left(\sqrt{\varepsilon_3} \mp n_3\right), \quad (3b)$$

where ε_3 is the relative dielectric constant of the electro-optic crystal for the polarization of the applied microwave field at the modulation frequency f_m, and c is the speed of light in vacuum. The first term of Eq. (3a) accounts for the contribution of the interaction with the co-propagating microwave, while the second term is associated with the counter-propagating microwave field.

Figure 68.26 shows a block diagram of the SSD modulator subsystem. Microwave pulses with peak powers in the kilowatt range and pulse lengths of several microseconds are generated by a mechanically tuned, triode microwave power oscillator. A ferrite circulator isolates the power oscillator from microwave drive power reflected from the SSD modulator, while a directional coupler is used to sample the incident and reflected power to the SSD modulator for system diagnostic purposes. A variable attenuator is included in the microwave circuit to control the drive-power level without changing the power oscillator operating point that can affect its operating frequency. A double-stub tuner is used to match the impedance of the modulator cavity to the 50-Ω coaxial cable that transmits the microwave drive power to the modulator.

Large phase amplitudes ($\eta \sim 3\pi$) are required to achieve the infrared laser bandwidths (~1.5 Å) from a single modulator required for successful implementation of 2-D SSD in laser-fusion experiments. To achieve these large phase amplitudes, thousands of volts must be applied across the electro-optic crystal at microwave frequencies. The microwave drive powers required to achieve these voltages in traveling-wave phase-modulator geometries are impractical, so resonant cavities are used to reduce the microwave drive-power requirements.

Two basic resonant cavity designs have been used for SSD phase modulators: radial-mode and reentrant coaxial-mode

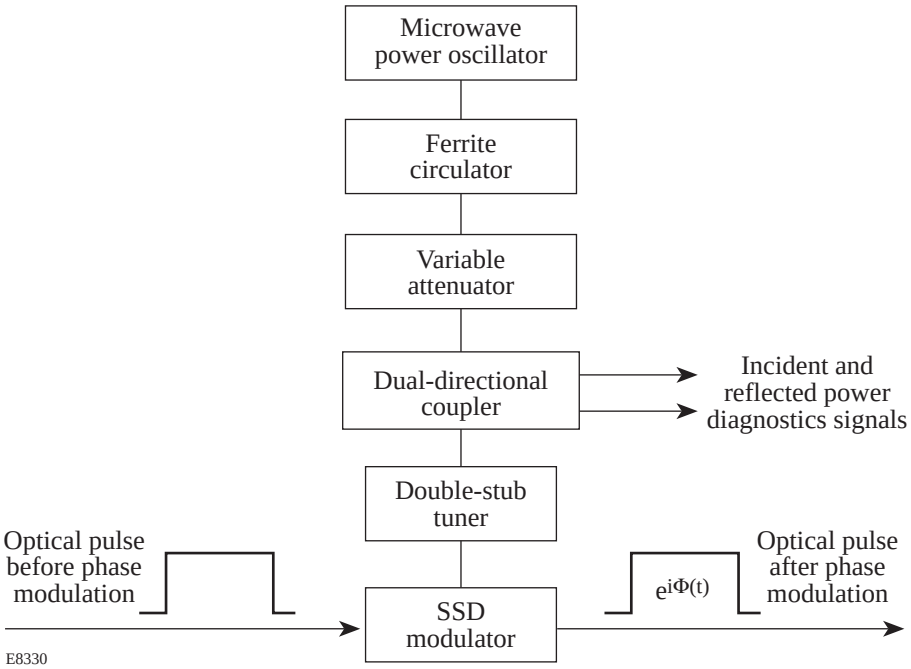

Figure 68.26
Block diagram of SSD modulator subsystem.

resonators. Early work at LLE was modeled after Kaminow's work[8] using radial-mode cavities with large crystals. In these designs, the diameter of the cavity is much larger than its overall height, and the electromagnetic wave inside the cavity propagates in the radial direction. Figure 68.27(a) shows a cutaway drawing of such a radial-mode cavity. Figure 68.27(b) illustrates a cross section of this modulator cavity along with the electric field distribution for a typical radial mode. The electric fields of this mode align with the symmetry axis of the cylindrical cavity, while the magnetic field lines are circular in horizontal planes. Microwave energy is coupled into the cavity using a magnetic loop antenna located on the outer wall of the cavity where the magnetic-flux density is a maximum.

As discussed later in **Computer Simulations Using *SUPERFISH***, spurious resonant modes can arise with resonance frequencies near the desired operating frequency. Additional difficulties with this design arise when the crystal dimensions approach the modulator cavity dimensions. Specifically, separate crystal resonance modes can exist above cutoff when the crystal thickness is nearly equal to the height of the cavity. Difficulties in efficiently coupling cavity-mode energy into the crystal mode prompted the use of highly reentrant coaxial cavities that proved to be significantly simpler to analyze and engineer.

A typical reentrant coaxial resonator is depicted in Fig. 68.28(a), which is essentially a section of coaxial transmission line that is short circuited at one end and capacitively loaded by the electro-optic crystal at the other end. The theory of reentrant coaxial resonators is discussed in many microwave references.[9–13] In this cavity geometry, predominantly transverse electromagnetic (TEM) waves propagate in the transmission-line section of the cavity, as shown in Fig. 68.28(b), while the fields at the capacitively loaded end conform to the end geometry. The electrode structures are made as large as possible, compared to the crystal size, to maximize the axial electric field uniformity in the electro-optic crystal. A magnetic loop antenna that couples microwave energy into the cavity is located near the center conductor at the short-circuited end of the transmission line.

The reentrant coaxial resonator design offers several advantages over the radial-mode designs. First, cavity-mode resonance frequencies are well separated, which simplifies excitation of only the desired cavity mode. Setting the resonance frequency is accomplished by machining the cavity length using analytical models that have been developed for this cavity design.

The dimensions of a reentrant coaxial resonator are determined by the properties of a coaxial transmission line. The impedance at a reference plane of a lossless, air-dielectric coaxial line of length L, with a characteristic impedance of Z_0 that is short circuited at its end, is given by[10]

$$Z_i = j\, Z_0 \tan\left(\frac{2\pi\, f_m\, L}{c}\right) (\text{ohms}), \qquad (4)$$

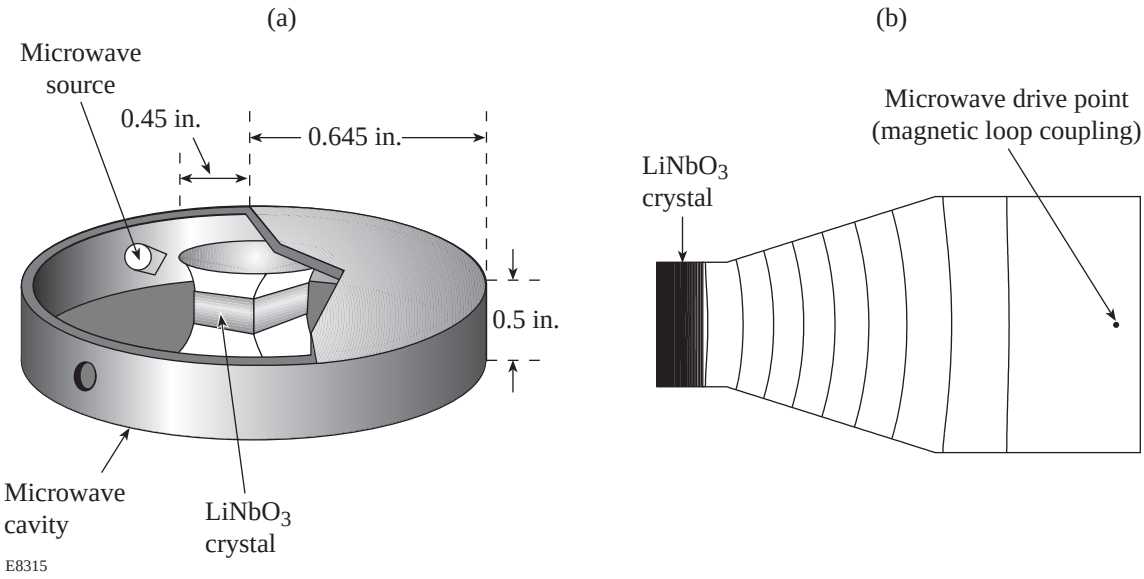

Figure 68.27
(a) Radial-mode cavity; (b) *SUPERFISH* field distribution.

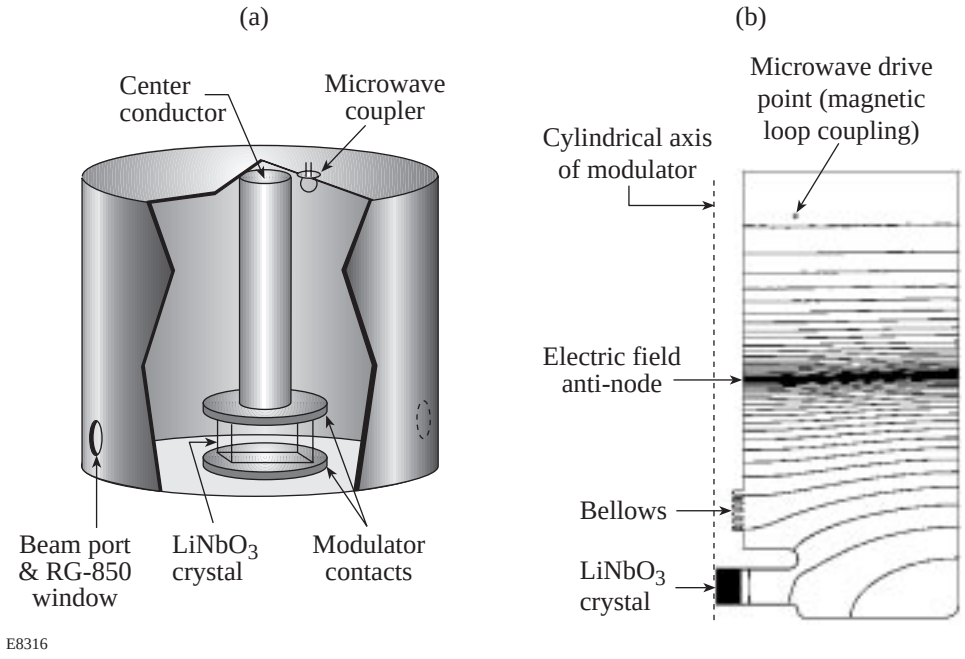

Figure 68.28
(a) Reentrant coaxial-mode cavity; (b) *SUPERFISH* field distribution.

where f_m is the microwave frequency and c is the speed of light. The characteristic impedance Z_0 can be calculated by the usual formula[11]

$$Z_0 = \frac{1}{2\pi}\sqrt{\mu/\varepsilon}\,\ln(b/a) \cong 60\ln\frac{b}{a}\ \text{(ohms)}, \tag{5}$$

where b is the inner radius of the outer conductor and a is the outer radius of the inner conductor.

By definition, resonance in a transmission-line cavity occurs when an external shunt reactance is connected to the transmission line that is equal to and opposite in sign to Z_i. For an open-circuited line, resonance occurs for values of f_m, which make the right-hand side of Eq. (4) infinite. This condition is satisfied when[10]

$$L = \left(\frac{2k-1}{4}\right)\lambda_m, \tag{6}$$

where k is any positive integer and $\lambda_m = c/f_m$ is the free-space wavelength of the microwave field. Equation (6) is the familiar odd-quarter-wave cavity length condition. Capacitively loaded lines can be treated with the same analysis to yield a "universal tuning curve." Since the reactance of the capacitor terminating the length of transmission line is given by

$$X_c = \frac{j}{2\pi f_m C}, \tag{7}$$

resonance occurs when Eqs. (4) and (7) are equal and opposite, leading to the analytic expression[10]

$$\tan\left(\frac{2\pi L}{\lambda_m}\right) = \frac{\lambda_m}{2\pi c\, C_{\text{total}}\, Z_0}. \tag{8}$$

The transmission line length normalized to the desired microwave wavelength λ_m is plotted in Fig. 68.29 versus this microwave wavelength normalized to the loaded transmission line characteristics. Equation (8) is a multivalued transcendental resonance condition with solutions for L, which are separated by $\lambda_m/2$.

This "universal tuning curve" determines the cavity length, given a known terminating capacitance, longitudinal mode number, and desired resonant frequency. Since the left-hand side of Eq. (8) repeats every half-wavelength, a resonance condition analogous to the odd-quarter-wavelength condition in Eq. (6) exists. Inspection of this curve shows that as the terminating capacitance approaches zero, the length of the resonator approaches one quarter of the free-space wavelength corresponding to the resonant frequency. As the capacitance becomes larger and larger, the length of the resonant cavity gets shorter. The 3/4 λ resonator mode is depicted in Fig. 68.28(b). It should be noted that the simplified analysis leading to Fig. 68.29 is not exact since stray capacitance due to fringing effects is difficult to quantify exactly.

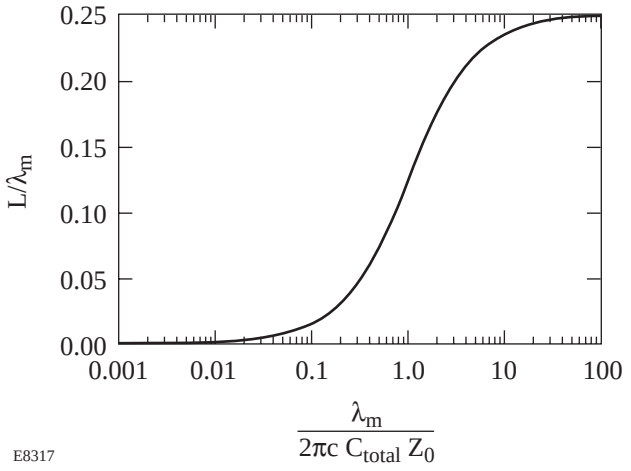

Figure 68.29
The "universal tuning curve" for reentrant coaxial resonators from Eq. (8) determines the cavity length of the $\lambda/4$ TEM mode of the modulator resonator. The cavity length of higher-order longitudinal modes is found by adding integer half-wavelengths.

Near resonance, a microwave cavity may be modeled as the parallel RLC resonant circuit shown in Fig. 68.30, where the shunt resistance R_s represents all of the losses in the cavity. Unfortunately, the appropriate definitions for R_s, L, and C are

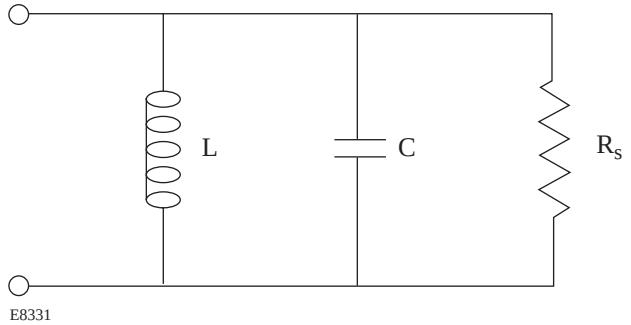

Figure 68.30
Near resonance, a resonant microwave cavity can be represented by an equivalent RLC circuit with a characteristic shunt impedance R_s.

somewhat ambiguous and arbitrary for a cavity resonator.[9] A more convenient set of parameters that totally describes the resonance is the cavity resonance frequency f_0, the "Q factor," and the shunt resistance R_s. For a given cavity mode, f_0 and the Q factor, or simply Q, are well-defined and can be calculated based on the size and shape of the cavity, as well as the materials and fabrication techniques employed in constructing the cavity. The definition of shunt resistance depends on the location where the voltage is defined, but it is conventional to define the path along which the electric field will be integrated to give the maximum voltage.[9] For SSD modulators, this corresponds to the voltage across the electro-optic crystal.

The Q of a resonant circuit or cavity is defined by[9]

$$Q = 2\pi\left(\frac{E_{\text{stored}}}{E_{\text{loss}}}\right), \tag{9}$$

where E_{stored} is the energy stored in the resonant cavity per cycle, and E_{loss} is the energy lost per cycle to conduction in the cavity walls and lossy dielectric materials inside the cavity. At a resonance frequency, the stored energy oscillates between the magnetic and electric fields. Since the electro-optic crystal in SSD modulators represents a capacitive load, a definition of stored energy in terms of the total capacitance of the modulator cavity is appropriate, and the stored energy is given by

$$E_{\text{stored}} = 1/2\, C_{\text{total}} V_{\text{peak}}^2, \tag{10}$$

where V_{peak} is the peak voltage achieved across the electro-optic crystal. The total cavity capacitance,

$$C_{\text{total}} = C_{\text{crystal}} + C_{\text{cavity}} + C_{\text{stray}},$$

is the sum of the capacitance due to the crystal, the cavity geometry, and stray capacitance due to fringing effects. Calculating the capacitances of the crystal and the cavity geometry is relatively straightforward, but estimating the stray capacitance can be quite difficult.

In the steady state, the energy lost per cycle is exactly balanced by the energy per cycle flowing into the cavity, so $E_{\text{loss}} = P_{\text{in}}/f$. Combining Eqs. (9) and (10) yields

$$V_{\text{peak}} = \sqrt{\frac{QP_{\text{in}}}{C_{\text{total}}\,\pi\, f}}, \tag{11}$$

which shows that minimizing the modulator capacitance is advantageous for generating the highest peak voltage across the crystal. In a general sense, a large-cavity Q factor also maximizes the voltage developed, although the effective shunt resistance of the cavity described below also plays an important role.

Assuming the crystal capacitance dominates the total modulator capacitance ($C_{\text{total}} \approx C_{\text{crystal}}$), the expression for a parallel plate capacitor ($C = \varepsilon WL/T$) can be combined with Eqs. (2) and (11) to yield

$$\eta^2 = \frac{\pi\, Q\, P_{\text{in}}}{\lambda^2\, \varepsilon_0\, f_m}\left(\frac{\beta^2}{WLT}\right)\left(\frac{n_3^6\, r_{33}^2}{\varepsilon_r}\right), \tag{12}$$

where $\varepsilon = \varepsilon_r \bullet \varepsilon_0$, ε_r is the relative dielectric constant, ε_0 is the dielectric constant of vacuum, and $W \cdot L \cdot T$ is the volume of the crystal, as depicted in Fig. 68.25. The first term is a constant for a given cavity design, modulation frequency, laser wavelength, and operating power. The second term depends only on the electro-optic crystal dimensions, although the phase-mismatch reduction factor β also depends on the material properties of the electro-optic crystal. It can easily be seen from Eq. (12) that small volume crystals are advantageous to achieving large phase-modulation amplitudes. The last term is a conventional figure-of-merit for electro-optic materials.

Assuming a sinusoidal voltage variation and steady-state conditions where the input power matches the average losses, or

$$P_{\text{in}} = V_{\text{peak}}^2 \big/ 2R_s, \tag{13}$$

the peak voltage developed in the cavity, V_{peak}, can be expressed as

$$V_{\text{peak}} = \sqrt{2\, P_{\text{in}} R_s}\,. \tag{14}$$

Equation (14) reveals the same square-root dependence on input power observed in Eq. (11); however, the coefficient now depends on the effective shunt impedance that is a function of cavity design. In some circumstances, maximizing the effective shunt resistance is more important than maximizing the Q factor when trying to achieve the highest voltages across the electro-optic material.

An important quantity in evaluating Q and R_s for a resonant cavity is the skin depth δ. At high frequencies, electromagnetic waves cannot penetrate deeply into conducting material.

The skin depth δ is defined as the depth at which the current density has fallen to l/*e* of its value at the surface, and it can be calculated from[14]

$$\delta = \sqrt{\frac{2}{\mu \omega_m \sigma}}, \tag{15}$$

where ω_m is the microwave angular frequency, σ is the conductivity of the material, and μ is the magnetic permeability of the material. For gold, the skin depth at 3.0 GHz is approximately 1.5 μm.

If dielectric losses in the electro-optic material can be neglected, then conduction losses in the metallic walls of the resonator represent the only losses in Eqs. (9) and (13), and both Q and R_s can be analytically evaluated by straightforward means for a capacitively loaded, reentrant coaxial cavity resonator to yield[9]

$$Q = \left(\frac{2z}{\delta}\right) \frac{\ln k}{2\ln k + z\left(\frac{k+1}{ka}\right)}, \tag{16}$$

and

$$R_s = 240\,\pi\, z^2 \frac{1}{\lambda_m \delta} \frac{\left[\ln(k)\right]^2}{2\ln(k) + z\left(\frac{k+1}{ka}\right)}, \tag{17}$$

where z is the inside height of the cavity, a is the radius of the center post, $k = b/a$ is the ratio of the inner cavity radius to the center post radius, λ_m is the free-space wavelength, and δ is the skin depth of the cavity material at the resonant frequency. Figure 68.31 shows Eqs. (16) and (17) plotted using dimensions for 3-GHz, gold-plated SSD modulators built for OMEGA. It can be seen that the shunt resistance calculated using this simplified model actually peaks for larger values of b/a than the Q factor. More exact calculations show that a maximum for the shunt resistance occurs when $z \approx (b–a)$, which corresponds to a square toroidal cross section.[9]

The utility of increasing the outer radial dimension of a cavity to maximize the shunt resistance is limited by the emergence of cavity modes with higher-order azimuthal variations. Figure 68.32 reproduces tuning curves for several of the TEM and TE_{11} modes of a reentrant-coaxial-cavity[10] to illustrate the difficulties created by degenerate cavity modes. The cavity resonance wavelength λ normalized to the cutoff wavelength λ_c for TE_{11} modes is plotted versus the normalized length of the coaxial section of the cavity, L/λ_c. For wavelengths shorter than the TE_{11} cutoff wavelength λ_c, numerous degenerate points exist between various TEM and TE_{11} modes, as indicated by the intersections marked with dots. For example, a common resonance wavelength is found for both the $\lambda_g/2$ TE_{11} mode and the $3\lambda/4$ TEM mode for one cavity length value. Degenerate modes, or nearly degenerate modes, degrade modulator performance since drive power may be coupled into another mode that does not exhibit a voltage maximum across the electro-optic crystal. Consequently, care must be taken in the cavity and coupling designs to excite only the desired cavity mode. A rule of thumb to identify the cavity dimensions at cutoff for these higher-order modes is that the mean circumference of the cavity, $L_{avg} = \pi(a+b)$, should be smaller than the desired free-space wavelength λ.[12]

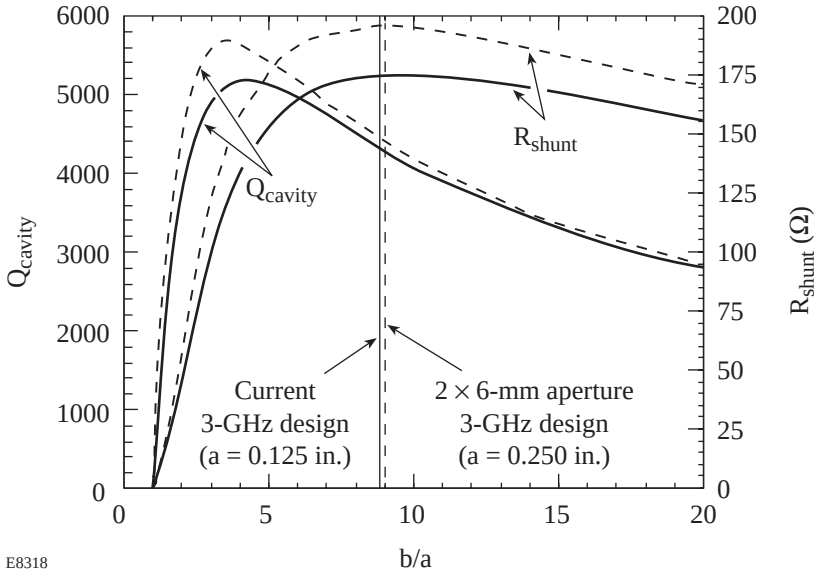

Figure 68.31
The approximate expressions for the cavity Q and shunt resistance for a reentrant coaxial-mode cavity exhibit peaks at different values for the ratio of the outer and inner radius, b/a. The solid lines represent the calculated values for the current, small-cavity 3.0-GHz modulator design (a = 0.125 in., b = 1.100 in., z = 2.000 in.), while the dashed lines are for the 2 × 6-mm aperture, large-cavity modulator (a = 0.250 in., b = 2.250 in., z = 2.170 in.). In both cases, the shunt resistance R_s is optimized.

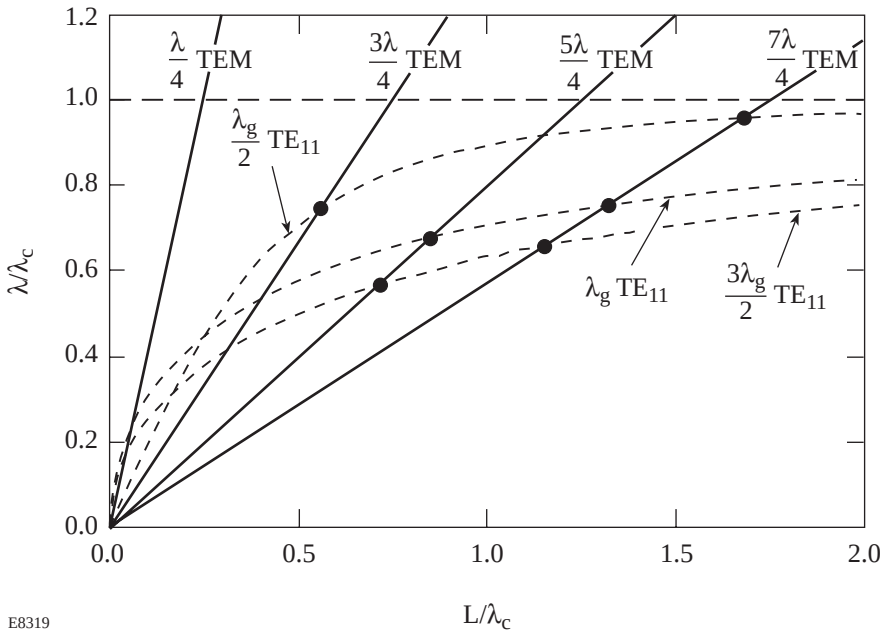

Figure 68.32
The tuning curves for several TEM and TE_{11} modes of a reentrant-coaxial-cavity illustrate the difficulties created by degenerate cavity modes (from Reich *et al.*[10]). The dots indicate degenerate points where two cavity modes have the same resonance wavelength for a given cavity length.

Computer Simulations Using *SUPERFISH*

Design and modeling of SSD modulators has been accomplished using the personal computer version of the *SUPERFISH* collection of programs developed at the Los Alamos National Laboratory.[15] The *SUPERFISH* package solves Maxwell's equations in two dimensions for both static magnetic and electric fields, as well as radio-frequency electromagnetic fields using finite element analysis. The codes analyze a user-defined cavity geometry to generate a triangular mesh that is subsequently used in the finite element analysis of the wave equation. Radio-frequency solvers iterate on the frequency and field calculation until finding a resonant mode of the cavity.

SUPERFISH numerical simulations of SSD modulators are limited to axially symmetric geometries. Given the rectangular geometry of the electro-optic crystal, SSD modulators are not strictly axially symmetric, but reasonably accurate results suitable for design purposes are achieved by modeling the crystal as a cylindrical crystal with an equivalent capacitance. The anisotropy of the $LiNbO_3$ crystals used in SSD modulators also cannot be modeled in *SUPERFISH*, but anisotropic effects should be minimal since the crystals are centered on the symmetry axis of the cavity where transverse fields should be very small.

Analyzing the field distributions of various cavity modes calculated by *SUPERFISH* is useful in identifying the optimal cavity design and drive frequency. Figure 68.33(a) displays a half cross section of the current-design OMEGA SSD modulator. Lines of constant electric field for the excited cavity mode are also shown, where the density of lines indicates the strength of the electric field. The electric fields of the standing wave in the transmission-line section of the cavity are essentially transverse, and a strong, axial electric field is observed in the electro-optic crystal between the electrodes, as expected from the analysis above.

Figure 68.33(b) shows the calculated radial dependence of the axial electric field component, E_z, in the equivalent cylindrical crystal at the three different horizontal positions shown in Fig. 68.33(a). Little variation is observed in the axial direction. Almost a 25% variation is calculated across the full radius of the equivalent cylindrical $LiNbO_3$ crystal, but smaller transverse variations are expected across the aperture of the actual rectangular $LiNbO_3$ crystal since the actual transverse dimensions are smaller. Of course, the exact field distribution is actually somewhat more complicated than calculated using this model since the $LiNbO_3$ crystal is actually a rectangular prism located in the center of an otherwise axially symmetric cavity. The calculated radial component of the electric field, E_r, is approximately 1000 times smaller than the axial electric field component, as expected from the symmetry of the modulator.

Figure 68.34(a) illustrates the electric field distribution of a new SSD modulator design currently being developed for the second stage of the two-dimensional SSD scheme implemented in OMEGA. A clear aperture with a larger dimension in the axial direction is required to accommodate a sweep of the laser beam at the second SSD modulator caused by the band-

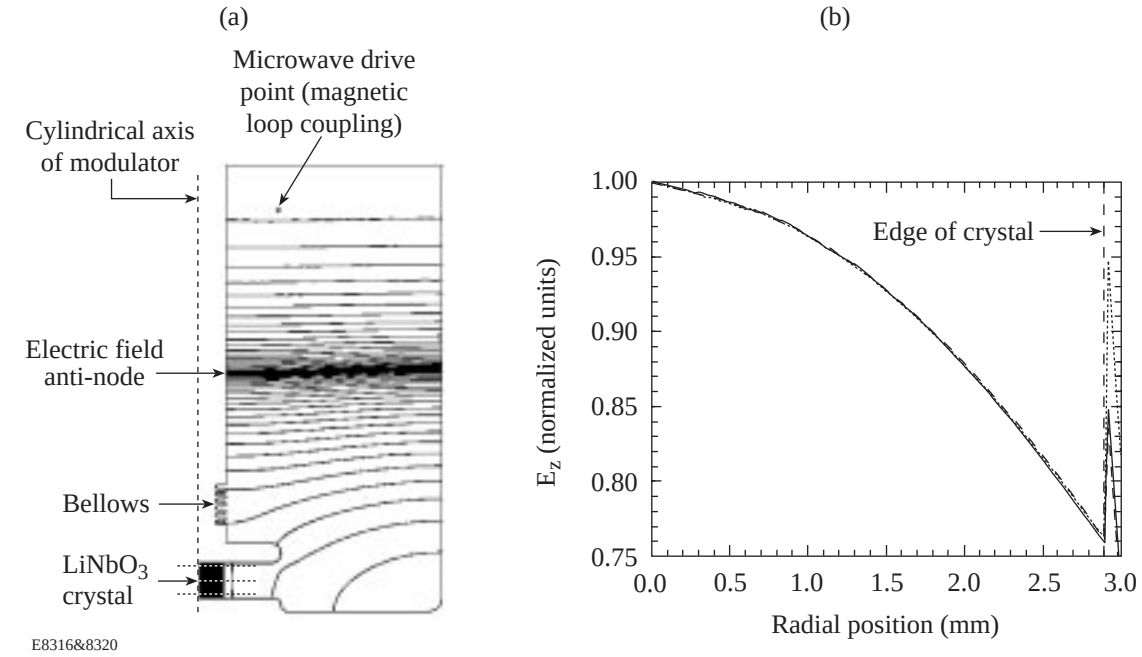

Figure 68.33
The electric field distribution for the small-cavity SSD modulator design. (a) A nearly TEM field distribution is observed in the "coaxial" section of the cavity. In this representation, the plotted field lines are parallel to lines of constant electric field and the electric field strength is related to the density of lines. (b) The radial dependence of the calculated electric field distribution is plotted for the three horizontal positions noted in Fig. 68.33(a). Little variation is observed among the three plots, but almost a 25% variation is predicted across the full radius of the equivalent cylindrical $LiNbO_3$ crystal. Smaller transverse variations are expected across the aperture of the actual rectangular $LiNbO_3$ crystal since the actual transverse dimensions are smaller.

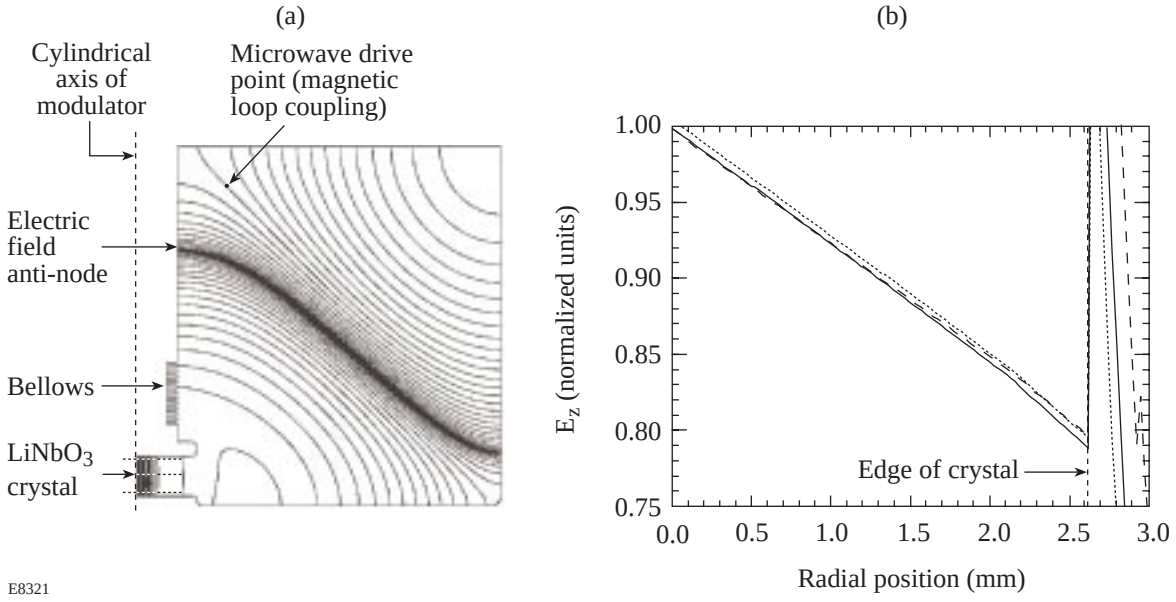

Figure 68.34
Electric field distribution for large-cavity SSD modulator. (a) The cavity mode is clearly not a TEM distribution in the "coaxial" section of the cavity; however, strong electric fields in the $LiNbO_3$ crystal are calculated, as represented by the high density of field lines. (b) The radial dependence of the calculated electric field distribution are plotted for the three horizontal positions noted in Fig. 68.34(a). Little variation is observed among the three plots, but approximately a 20% variation is predicted across the full radius of the equivalent cylindrical $LiNbO_3$ crystal.

width and dispersion introduced in the first stage of SSD. The aspect ratio b/a for this modulator is similar to the current design depicted in Fig. 68.33(a), but the larger radial dimensions lead to somewhat higher values for Q and R_s, as shown in Fig. 68.31. This new design was pursued with the goal of generating larger voltages across the electro-optic crystal required to achieve the same electric field strengths as in the current design.

The electric field distribution of the cavity mode displaying the strongest fields in the $LiNbO_3$ crystal is shown in Fig. 68.34(a). It differs remarkably from the current SSD modulator design in that the electric fields clearly are not transverse in the "transmission line" section of the cavity. Strong, relatively uniform axial components of the electric field in the crystal are calculated, as shown in Fig. 68.34(b), indicating that this design should be suitable for SSD operation. Compared to the small-cavity modulator design, the smaller transverse dimension of the $LiNbO_3$ crystal aperture should produce even smaller radial variations. Again, the calculated radial component E_r was found to be negligible compared to the axial component.

Experimental tuning curves for cavity modes of the large-cavity SSD modulator were measured by adjusting the cavity length of the resonator with aluminum shim plates between the cover assembly and cavity body. These measured resonance frequencies are compared in Fig. 68.35 with resonance frequencies numerically calculated by *SUPERFISH*. The numerical and measured tuning curves for this design agree remarkably well, but they depart substantially from the analytical form given by Eq. (8). This departure confirms that the actual modes of this modulator cavity are not consistent with the TEM mode analysis used to derive Eq. (8).

The lowest-frequency cavity mode tracked as a function of cavity length corresponds to a nearly radial mode, while the next higher frequency matches the calculated tuning curve for the nearly axial mode shown in Fig. 68.34(a). Both of these modes were reproduced by the *SUPERFISH* simulations, which predict the tuning variations with reasonable accuracy; however, three additional, higher-frequency cavity modes are experimentally observed that cannot be reproduced by any axially symmetric *SUPERFISH* solutions. Two nearly degenerate resonance modes appear that are most likely two similarly shaped modes that are slightly perturbed by the rectangular symmetry introduced by either the $LiNbO_3$ crystal or the magnetic coupling loop. The measured tuning curves for these modes actually cross the tuning curve for the nearly axial mode in two places, effectively preventing efficient operation near the desired 3.3-GHz SSD modulator frequency since each of these cavity modes would be excited by the drive power. The desired mode can be excited at the 3.0-GHz SSD modulator frequency since the resonance frequencies for these nearly degenerate modes are well separated by about 100 MHz. The highest-frequency mode most likely represents a first-order azimuthal mode of the cavity since it is relatively insensitive to cavity length until it approaches cutoff at the shortest cavity lengths investigated.

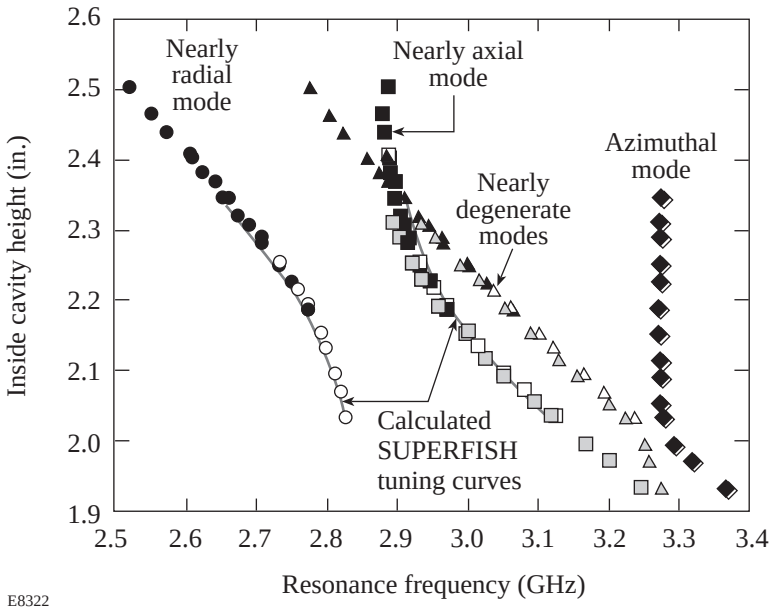

Figure 68.35
Measured and numerically simulated (*SUPERFISH*) tuning curves are plotted as a function of cavity length for large-aperture SSD #2 cavity.

Design Criteria

Numerous considerations impact the design and construction of SSD phase modulators, including laser-irradiation uniformity and OMEGA laser system damage considerations, as well as optical, electrical, and mechanical considerations. Each of these items is discussed in more detail below.

1. Uniformity and Laser System Considerations

The required SSD bandwidth is dictated by fusion target physics that have been addressed in previous SSD publications[16] and will not be treated in detail here. In general, large bandwidths are desirable, but laser system considerations, such as efficient frequency conversion to the third harmonic[17] and avoiding pinhole closure in the vacuum spatial filters, currently limit the useful bandwidth requirements to approximately 3 Å, given the current SSD grating dispersion.

Modulator frequency is determined by several irradiation uniformity issues. First, the microwave modulation period should be of the order of the effective smoothing time required to minimize imprinting of instantaneous laser speckle patterns on laser-fusion targets.[16] For two-dimensional SSD, a second constraint is that the modulator frequencies should be incommensurate (3.0 and 3.3 GHz) to maximize the number of individual lines within the SSD spectrum. Lastly, achievable phase-modulation amplitudes also impose a practical constraint on modulator frequency since the required SSD bandwidth is related to the modulation frequency by $\Delta\nu = 2\eta f_m$.

2. Optical Considerations

Lithium niobate ($LiNbO_3$) and potassium titanyl phosphate (KTP) are two commercially available electro-optic materials suitable for SSD modulators. Values for the relevant optical parameters of these materials are reported in Table 68.III. Both crystals possess large electro-optic coefficients suitable for transverse modulator geometries. KTP boasts higher r_{33} values and laser damage thresholds than $LiNbO_3$, but the electro-optic figure-of-merit in Eq. (12) is higher for $LiNbO_3$. All of the SSD modulators designed and built at LLE to date are based on $LiNbO_3$.

Damage threshold values reported in the literature vary quite widely depending on the purity and cleanliness of the material and antireflection coatings applied to the crystals. Most of these damage thresholds are reported for long pulses typically greater than 10 ns and must be scaled to the pulse lengths appropriate for laser-fusion experiments that are between 800 ps and several nanoseconds using an $I_{\text{damage}} \propto \sqrt{t_{\text{pulse}}}$ scaling law. Independent damage testing of $LiNbO_3$ at LLE has demonstrated damage thresholds greater than 1 GW/cm^2.

$LiNbO_3$ exhibits a photorefractive damage mechanism when exposed to visible and ultraviolet light. The scattering and absorption associated with this mechanism reduce the transmission of the crystal and may alter phase-modulation efficiency. To avoid this problem, room lights and flash lamps are blocked from the SSD modulators by windows made from

Table 68.III: Material parameters for $LiNbO_3$ and KTP.

	$LiNbO_3$	KTP
Electro-optic coefficient (pm/V)	r_{33} = 28.8–30.8 (at 633 nm)[18]	35.0
Index of refraction	n_3 = 2.1561 (extraordinary)	1.80
Relative dielectric constant	ε_{33} = 23.7–27.9[18]	15.4
$\frac{n_3^6 r_{33}^2}{\varepsilon_r}(\text{pm/V})$ (using average values)	3304	2705
Laser damage threshold (1-ns pulse, λ = 1.06 μm)	1.2 GW/cm^2	>1 GW/cm^2

long-pass optical filter glass (RG-850), although two-photon absorption of intense infrared laser pulses may still pose a problem.[18] MgO-doped $LiNbO_3$ has been shown to prevent accumulation of photorefractive damage[19] and may be pursued for SSD modulators if this nonlinear mechanism proves active in the current design.

Electro-optic crystal dimensions are critically related to both the optical and microwave performance of SSD modulators. The cross-sectional area, or clear aperture of the modulator, is principally determined by laser-damage considerations. In OMEGA, SSD modulators are located in the driver line where 1- to 5-ns pulses with energies of approximately 10 to 100 mJ per pulse are typical. Designing for the worst case (1 ns, 100 μJ), a minimum beam diameter of approximately 110 μm corresponds to the damage threshold of 1 GW/cm^2. For conservatism, the actual beam diameter in the OMEGA driver line is set to approximately 400 μm. The minimum clear aperture of the crystal is chosen to be about five times larger than the beam diameter to account for misalignment and fabrication tolerances, as well as chamfers on the edges of the crystal to avoid breakage during grinding and polishing, which leads to a minimum clear aperture of 2 mm. A rectangular cross section (3 mm wide and 4 mm high) is used in SSD modulators currently in operation in OMEGA since experience learned over several years of developing and testing modulators empirically shows that square cross sections seem to lead to dielectric resonance modes that can interfere with the desired mode of a cavity.

Another factor that determines the cross-sectional size of the crystal in the second SSD modulator used in two-dimensional SSD is the bandwidth and dispersion impressed on the laser beam by the first stage of SSD. The restoration grating of the first SSD stage and the delay grating of the second SSD stage introduce 440 μrad/Å of dispersion in the horizontal and vertical directions, respectively. Since the second SSD modulator is located at the focal plane of a long-focal-length lens ($f = 3062$ mm), the beam sweeps through a distance of approximately ±2 mm at the second modulator when the first modulator operates at the design bandwidth of $\Delta f_1 = 1.5$ Å. Due to the two orthogonal gratings in series, the sweep of the focal spot is oriented at 45° with respect to the horizontal, as shown in Fig. 68.36. To account for this sweep, a new SSD #2 modulator is currently being developed with a clear aperture of 2×6 mm.

The maximum crystal length is determined by phase-mismatching between the laser and microwave fields in the

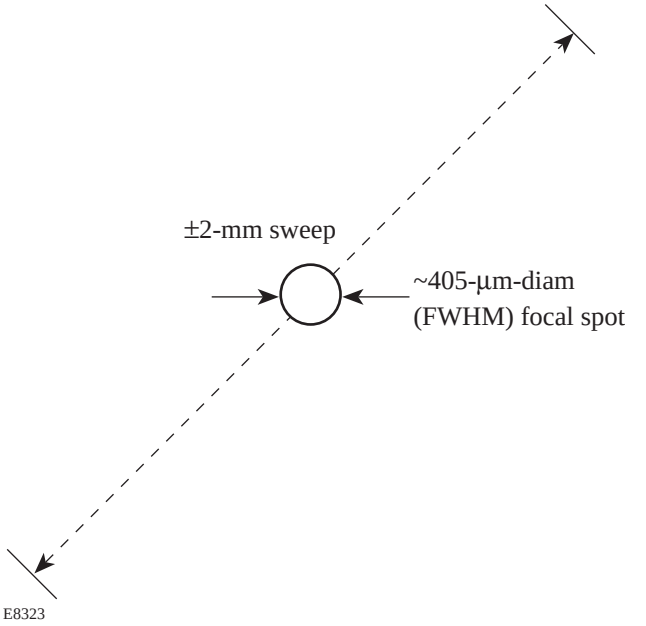

Figure 68.36
Clear-aperture requirements for SSD modulators are based on damage thresholds and beam sweep at focal plane of second SSD modulator in 2-D SSD.

$LiNbO_3$ crystal as determined by Eq. (3). The product of the phase-matching reduction factor and the $LiNbO_3$ crystal length β_L appearing in Eq. (2) is plotted in Fig. 68.37 versus crystal length for SSD modulators operating at both 3.0 and 3.3 GHz. The optimal length for these frequencies is observed to be approximately 10 and 9 mm, respectively. For simplicity, a 9-mm-long crystal is used in both the 3.0- and 3.3-GHz small-cavity modulators, while the 3.0-GHz large-cavity modulator uses an 11-mm-long crystal.

Another constraint is the maximum force that can be exerted on the crystal. Tests in interferometers and polarimeters show that the maximum allowable pressure on the crystal is about 750 g/cm^2 for $LiNbO_3$ before any noticeable changes take place in transmitted wavefront or residual retardance.

Proper crystal alignment with respect to the laser-beam polarization and propagation is critical since the tensor electro-optic properties of $LiNbO_3$ lead to a time-varying birefringence in the geometry used for SSD modulators that can generate amplitude modulation in polarization elements in the laser system. Proper alignment is also important in eliminating second-harmonic generation in the crystal since $LiNbO_3$ also possesses a strong $\chi^{(2)}$ coefficient. The laser polarization angle θ_y in the plane perpendicular to propagation, shown in

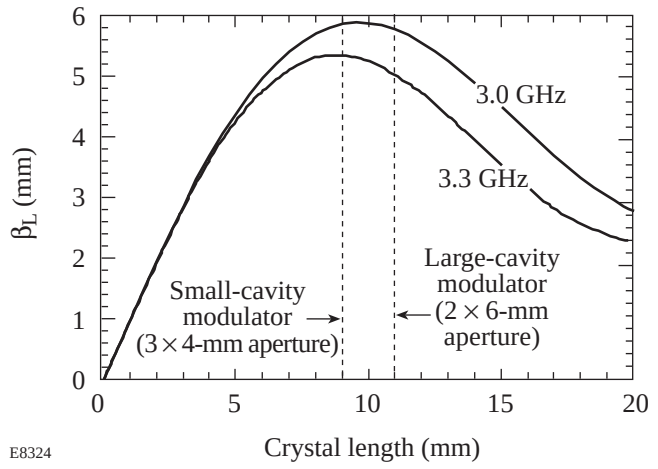

Figure 68.37
The product of the phase-matching reduction factor and the $LiNbO_3$ crystal length β_L appearing in Eq. (2) is plotted for both the 3.0- and 3.3-GHz SSD modulator frequencies. A maximum for these two frequencies appears between 9 and 10 mm. The small-cavity 3.0- and 3.3-GHz modulators utilize a 9-mm-long crystal, while the large-cavity 3.0-GHz modulator uses an 11-mm-long crystal.

Fig. 68.25, is easily controlled with a half-wave plate, while the pitch and yaw angles θ_x and θ_z, respectively, are controlled by mounting the modulator on goniometer stages with the center of rotation located at the center of the $LiNbO_3$ crystal.

3. Electrical Considerations

High-power, tunable microwave oscillators and transmission components are commercially available in the standard microwave bands of interest for SSD modulators listed in Table 68.IV. Surplus radar equipment is particularly attractive since high-power equipment is often available at reasonable prices. Given a cavity Q factor of approximately 1000, input powers of the order of several kilowatts are required to achieve the phase-modulation amplitudes required for SSD applications in inertial confinement fusion.

The coupling loop design is important for efficiently exciting the desired resonant cavity mode. To minimize the perturbation on the cavity mode caused by the coupling loop, its dimensions should be small compared to the microwave wavelength, which is approximately 10 cm at frequencies near 3 GHz. The loop is oriented perpendicular to the magnetic fields of the cavity to efficiently couple the microwave energy from the coaxial transmission line to the cavity mode. A low-resistance loop fabricated from gold-plated wire minimizes resistive losses.

Table 68.IV: U.S. military microwave bands.[20]

Microwave Band	Frequency (GHz)
S	1.550–3.900
X	6.200–10.900
K	10.900–36.000

The size of the coupling loop is determined empirically by approximately matching the complex impedance of the loop in the cavity to the characteristic impedance of the 50-Ω coaxial transmission line. Final impedance matching is accomplished using a standard double-stub tuner to minimize the power reflected from the modulator. Reflected power signals more than 30 dB below the incident power are easily achievable with careful coupling loop design and impedance matching.

The modulator cavity bodies are normally machined from solid stock to minimize the number of joints that would otherwise increase losses. The cavities built at LLE have usually been machined from high-purity copper in order to attain the highest conductivity possible. Several skin depths of gold are electroplated on the cavity to avoid oxidation of the surface that would increase conduction losses and reduce cavity performance. Gold-plated brass and silver-plated stainless steel have also been used. Machining tolerances are not stringent, but surface finish is very important. To minimize microwave losses, the surface finish must be an order of magnitude better than the skin depth. A skin depth of 1.5 μm is calculated from Eq. (15) at 3 GHz for gold, which indicates that sub-micron surface finishes are desirable. Single-point diamond machining of copper cavities followed by mechanical polishing yields a near-mirror finish.

Center posts are soldered to the covers, and numerous bolts are used to join this assembly to the resonator cavity body to insure a low-loss connection. An indium "o-ring" has also been employed in some modulators to ensure excellent electrical contact between the cover and the resonator cavity body. An adjustable, spring-loaded bellows is used to provide a controllable clamping force on the electro-optic crystal. A bellows is used, rather than a sliding joint, to maximize the conductance through the clamping assembly.

The most important electro-mechanical constraint in the cavity design is the electrical connection between the resonator and the electro-optic crystal. A low-loss connection is critical since very large microwave currents are delivered to the crystal. Gold-on-chromium electrodes are vapor deposited on the

$LiNbO_3$ crystal. A long-lasting, high-conductance contact to the crystal electrodes is accomplished using an gallium/indium alloy near the eutectic point for this material system (~85.8% Ga, 14.2% In) that has a liquid-solid transition temperature just above room temperature. After the cavity components, the crystal, and a crucible of the GaIn alloy are all heated above this temperature, the molten alloy is spread on the crystal electrodes and on the contact surfaces of the cavity. Great care is taken to ensure continuous coverage and complete wetting of the metallic surfaces. The modulator is assembled at this elevated temperature, and the spring pressure is adjusted to provide the correct clamping force on the crystal. Plastic alignment jigs are used to center the crystal in the cavity. The modulator is slowly returned to room temperature to allow the residual stress due to differential thermal contraction between the metal of the cavity and the $LiNbO_3$ to be taken up by the GaIn alloy. It can take several days for the alloy to completely harden, so mechanical shock must be avoided.

Arcing can occur between the modulator contacts at high microwave drive powers since strong electric fields can be developed in the modulator cavity. When this arcing limits the achievable bandwidth from the modulators, the cavities have been designed to operate in vacuum. Indium o-ring seals provide a good electrical contact between the cover and the body.

Testing

Modulator electrical performance can be accurately evaluated using a modern, vector network analyzer, such as the HP 8720B. The reflected power coefficient S_{11} for a modulator can be measured across a range of excitation frequencies and plotted in several convenient formats. Figure 68.38(a) shows S_{11} for a 3-GHz modulator. Optimizing the coupling loop dimensions and impedance matching minimize the reflected power at the resonance frequency. This corresponds to matching the resistive part of the modulator's complex impedance as close as possible to the 50-Ω coaxial line used to transmit drive power to the modulator, and minimizing the reactive part. The complex impedance $Z = R + jX$ of the modulator at the different excitation frequencies can also be represented in the format shown in Fig. 68.38(b). Careful coupling loop design can nearly achieve this condition, but final impedance matching is accomplished with a double-stub tuner.

The unloaded "Q" of the modulator can be estimated by

$$Q_{\text{unloaded}} \approx \frac{f_m}{\Delta f} = \frac{f_m}{f_2 - f_1}, \qquad (18)$$

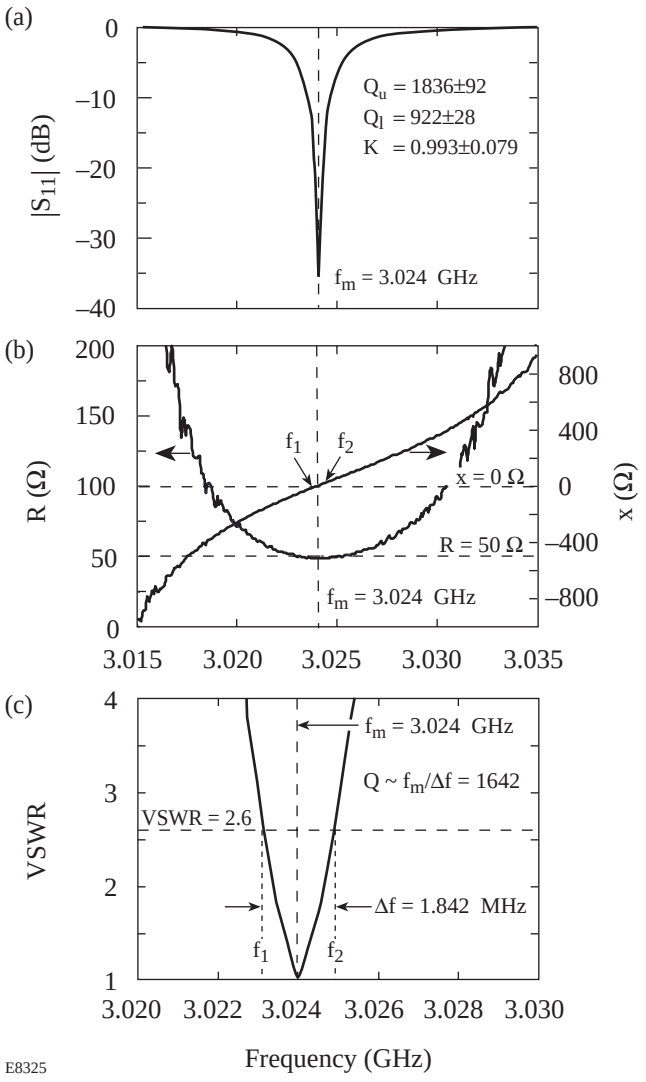

Figure 68.38
Electrical performance of large-cavity 2 × 6-mm aperture, 3.0-GHz modulator measured using the HP 8720B vector network analyzer. (a) The reflection coefficient $|S_{11}|$ plotted versus the excitation frequency demonstrates the narrow resonance of the modulator cavity. (b) The frequency difference between the points where the resistive and reactive parts have equal magnitude can be used in Eq. (18) to estimate the Q-factor of the resonant cavity. (c) The VSWR dependence on excitation frequency can also be analyzed to yield an estimate of the Q-factor by finding the frequency difference between the points where the VSWR is 2.6 times the value at f_m.

where f_m is the resonance frequency and Δf is the difference between the two frequencies that correspond to the point where the complex impedance is equally resistive and reactive. These two frequencies are denoted in Fig. 68.38(b) by points 1 and 2.

Another graphical approach using Eq. (18), which is equivalent to the method described above, estimates the unloaded Q of the modulator cavity using the voltage-standing-wave-ratio (VSWR) plotted versus excitation frequency, as shown in Fig. 68.38(c). In this method, the denominator in Eq. (18) is the difference between the two frequencies, f_1 and f_2, at which the VSWR is a factor of 2.6 times the value at f_m.

More exact values for Q_{unloaded} can be developed by numerically curve fitting Fig. 68.38(a) or 68.38(b) to the corresponding analytic expression using an algorithm such as implemented in the program QZERO.[21] QZERO also determines Q_{loaded}, the coupling coefficient K, and the uncertainty in each parameter, which are noted in Fig. 68.38(a).

High-power bench-top testing is useful to confirm proper coupling of the microwave drive power into the modulator cavity, as well as to identify potential low-resistance paths that might shunt power away from the electro-optic crystal, or "cat whiskers," formed by the GaIn solder that might cause premature arcing between the cavity electrodes.

Final optical testing is performed by passing prototypical laser pulses through the modulator to measure the bandwidth added by the modulators. A Fabry-Perot spectrometer is employed to measure the optical bandwidth of the laser pulse. Figure 68.39(a) shows the Fabry-Perot fringes captured by a video camera. Three fringes are observed that correspond to different transmission orders of the Fabry-Perot etalon. The width of each fringe corresponds to the optical bandwidth of the laser pulse, which can be calculated using the parameters of the etalon. Figure 68.39(b) depicts this optical bandwidth from which the full-width-at-half-maximum (FWHM) instrumental resolution is estimated to be approximately 0.2 Å.

Figure 68.40 presents the optical bandwidth measurements for the small-cavity 3.3-GHz modulator. Figure 68.40(a) shows the Fabry-Perot fringes that can be analyzed to yield the optical bandwidth shown in Fig. 68.40(b). For this modulator, 3.5 kW of microwave drive power yield approximately 1.49 Å of bandwidth. A convenient rule-of-thumb for estimating the SSD bandwidth in this experimental setup is given by the full width at 70% of the maximum, which very closely corresponds to the SSD bandwidth defined by $\Delta\lambda = \pm\eta\, f_m$. The dashed line in Fig. 68.40(b) represents the calculated Fabry-Perot spectrum for this estimated SSD bandwidth. Using this bandwidth measurement and the material properties in Table 68.III in Eqs. (2), (3), and (13) for this modulator, a value for the shunt impedance $R_s \approx 10\ \text{k}\Omega$ is calculated. Figure 68.41 shows the Fabry-Perot fringes and calculated spectra for the large-cavity 3.0-GHz SSD modulator.

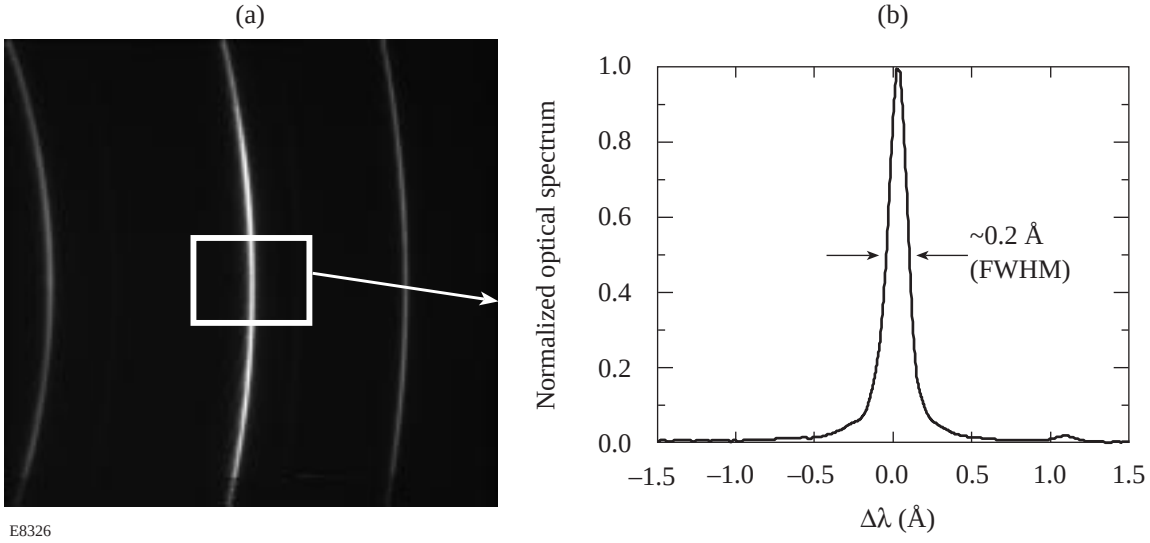

Figure 68.39
(a) Video image of Fabry-Perot fringes for laser pulse without SSD modulator energized. (b) Fabry-Perot fringes converted to a wavelength scale show that the instrumental response is approximately 0.2 Å.

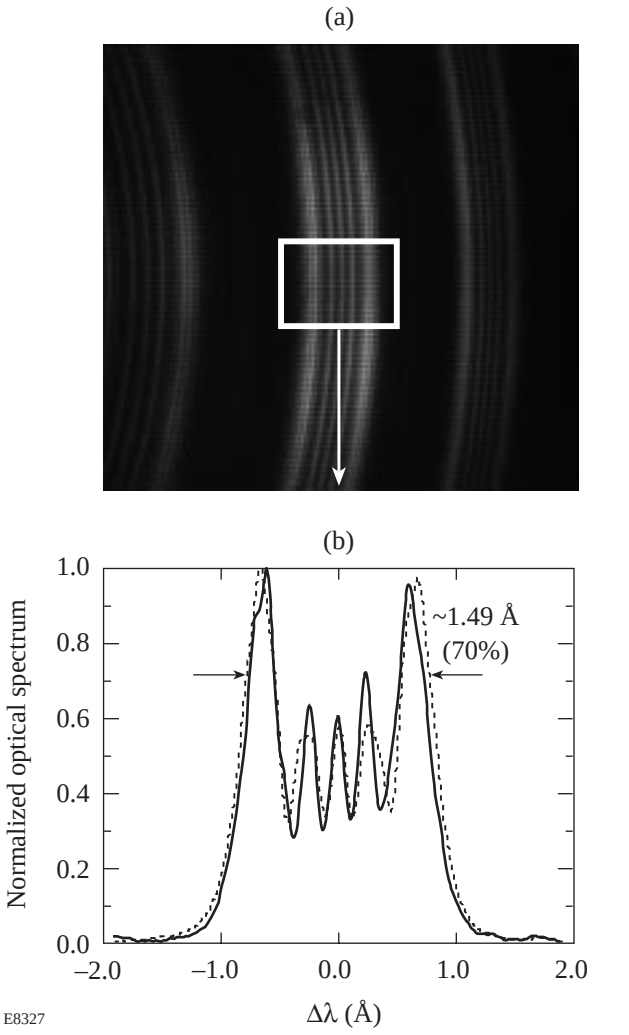

Figure 68.40
(a) Spectral measurements for the small-cavity 3.3-GHz SSD modulator depicted in Fig. 68.33 are made with a Fabry-Perot interferometer. The width of the fringes corresponds to the bandwidth of the laser beam, while the spacing between the fringes represents the free spectral range of the interferometer. (b) The Fabry-Perot fringes converted to a wavelength scale shows that approximately 1.49 Å of bandwidth was added to the laser beam with 3 kW of microwave drive power. The simulated spectrum for this phase modulation amplitude is shown as a dashed line.

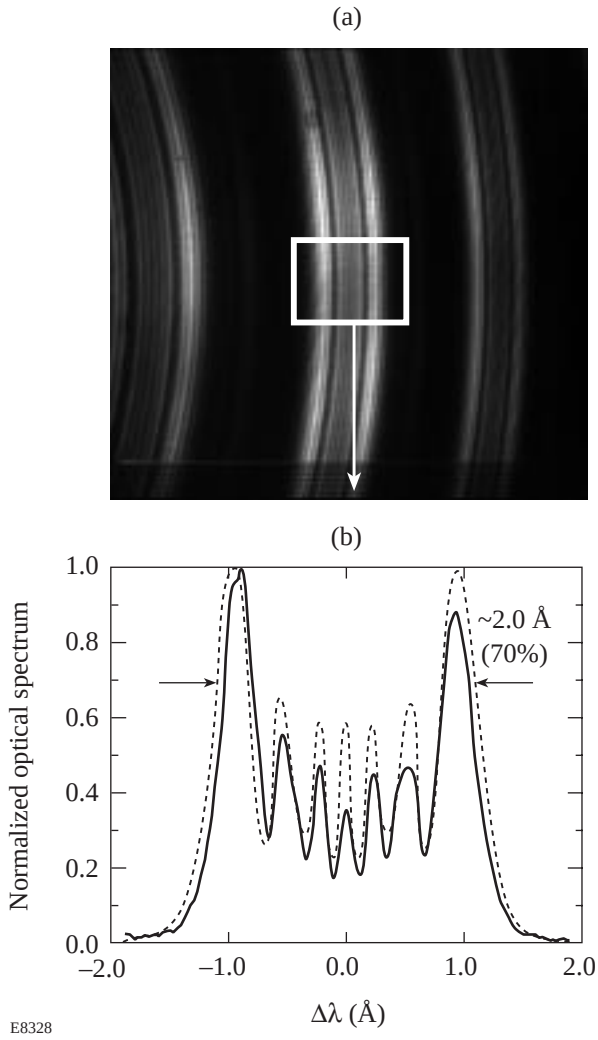

Figure 68.41
Pulsed Fabry-Perot spectra for large-aperture 3.0-GHz, large-cavity SSD modulator shown in Fig. 68.34. (a) Fabry-Perot interferometer fringes. (b) The Fabry-Perot fringes converted to a wavelength scale shows that approximately 2.0 Å of bandwidth was added to the laser beam with 5 kW of microwave drive power. The simulated spectrum for this level of phase modulation is shown as a dashed line.

Conclusions

Microwave phase modulators have been employed in various SSD configurations on OMEGA. The current modulator designs are $LiNbO_3$-based devices with microwave drive powers enhanced by resonant cavities. Large single-pass bandwidths are achieved in these modulators that provide substantial improvements in laser-irradiation uniformity.

Further improvements in uniformity are possible with higher-frequency SSD modulators that can generate significantly larger bandwidths. Advanced generations of modulator designs are presently under investigation, including multipass modulators, quasi-phase-matched modulator structures to compensate for the phase mismatching between the optical and microwave fields, and alternate electro-optic materials.

ACKNOWLEDGMENT

This work was supported by the U.S. Department of Energy Office of Inertial Confinement Fusion under Cooperative Agreement No. DE-FC03-92SF19460, the University of Rochester, and the New York State Energy Research and Development Authority. The support of DOE does not constitute an endorsement by DOE of the views expressed in this article.

REFERENCES

1. R. T. Denton, F. S. Chen, and A. A. Ballman, J. Appl. Phys. **38**, 1611 (1967).
2. M. A. Duguay and J. W. Hansen, IEEE J. Quantum Electron. **QE-4**, 477 (1968).
3. M. A. Duguay and J. W. Hansen, Appl. Phys. Lett. **14**, 14 (1969).
4. Laboratory for Laser Energetics LLE Review **37**, NTIS document No. DOE/DP/40200-83, 1988 (unpublished), p. 29.
5. Laboratory for Laser Energetics LLE Review **37**, NTIS document No. DOE/DP/40200-83, 1988 (unpublished), p. 40.
6. A. Yariv, *Quantum Electronics* (Wiley, New York, 1975), Sec. 14.4.
7. I. P. Kaminow and J. Liu, Proc. IEEE **51**, 132 (1963).
8. I. P. Kaminow and W. M. Sharpless, Appl. Opt. **6**, 351 (1967).
9. T. Moreno, *Microwave Transmission Design Data* (Dover Publications, New York, 1948).
10. H. J. Reich, J. G. Skalnik, P. F. Ordung, and H. L. Krauss, *Microwave Principles* (D. Van Nostrand Company, Princeton, NJ, 1957).
11. F. E. Gardiol, *Introduction to Microwaves* (Artech House, Dedham, MA, 1984).
12. G. J. Wheeler, *Introduction to Microwaves* (Prentice-Hall, Englewood Cliffs, NJ, 1963).
13. J. C. Slater, *Microwave Electronics* (D. Van Nostrand Company, New York, 1950).
14. J. D. Jackson, *Classical Electrodynamics*, 2nd ed. (Wiley, New York, 1975).
15. L. M. Young and J. H. Billen, computer code *SUPERFISH* (Los Alamos National Laboratory, Los Alamos, NM, 1996). (The *SUPERFISH* computer code is located on the Internet at http://www-laacg.atdiv.lanl.gov/c-on-line/descriptions/superfpc.html)
16. S. Skupsky, R. W. Short, T. Kessler, R. S. Craxton, S. Letzring, and J. M. Soures, J. Appl. Phys. **66**, 3456 (1989).
17. M. D. Skeldon, R. S. Craxton, T. J. Kessler, W. Seka, R. W. Short, S. Skupsky, and J. M. Soures, IEEE J. Quantum Electron. **28**, 1389 (1992).
18. R. S. Weis and T. K. Gaylord, Appl. Phys. A **37**, 191 (1985).
19. D. A. Bryan *et al.*, Opt. Eng. **24**, 138 (1985).
20. S. Y. Liao, *Microwave Devices and Circuits* (Prentice-Hall, Englewood Cliffs, NJ, 1980).
21. D. Kajfez, *Q Factor* (Vector Fields, Oxford, MS, 1994).